This version of the manuscript is the final revised one of the published on-line
https://doi.org/10.1016/j.canlet.2019.02.013

Caveolin-1 enhances metastasis formation in a human model of embryonal rhabdomyosarcoma through Erk signaling cooperation

Silvia Codenotti[a], Fiorella Faggi[a], Roberto Ronca[a], Paola Chiodelli[a], Elisabetta Grillo[a], Michele Guescini[b], Francesca Megiorni[c], Francesco Marampon[d], Alessandro Fanzani[a,*]

[a] *Department of Molecular and Translational Medicine, University of Brescia, Brescia, Italy*

[b] *Department of Biomolecular Sciences, University of Urbino Carlo Bo, Urbino, Italy*

[c] *Department of Pediatrics, "Sapienza" University of Rome, Rome, Italy*

[d] *Department of Radiotherapy, Policlinico Umberto I, "Sapienza" University of Rome, Rome, Italy*

A B S T R A C T

Rhabdomyosarcoma (RMS) is a pediatric soft tissue tumor classified in two major subtypes namely embryonal and alveolar, which have distinctive histopathological and genetic signatures and worse outcomes in the pre- sence of metastases. Here, in order to evaluate the role of Caveolin-1 (Cav-1) in embryonal RMS dissemination, we employed an experimental in vivo metastasis assay using immunodeficient NOD/SCID mice. We found that the intravenous injection of human RD cells engineered for Cav-1 overexpression promoted the formation of lung metastases compared to parental cells. The arisen metastases were isolated and cultured in vitro to establish two derivative lines that showed greater metastatic capacity, as detected by performing in vivo metastasis and tumor spheroid invasion assays. Compared to parental cells, all metastatic lines were characterized by an increase in cell proliferation, migration and invasiveness that were downregulated by synthetic inhibition of Erk pathway. The metastatic cells showed a marked cell apoptosis induced by nutrient deprivation and consistent loss of differentiation characterized by depletion of MyoD and Myogenin factors. Furthermore, they showed marked changes in cell size, a re-organization of the three-dimensional cytoskeleton characterized by an increased actin stress fiber content, and increased adhesion and angiogenic properties. Collectively, these data provide new insights into Cav-1-driven metastatic process of embryonal RMS through cooperation of the Erk signaling pathway. Furthermore, our derivative metastatic lines represent useful tools for identifying genes or molecular pathways that regulate the metastatic progression of embryonal RMS.

1. Introduction

Rhabdomyosarcoma (RMS) is a myogenic tumor that accounts for approximately 50% of all pediatric soft tissue sarcomas. Diagnostic criteria for RMS base on the validation of proteins of the skeletal muscle lineage, such as Desmin, MyoD or Myogenin [1]. RMS cells are per- sistently kept in a proliferation state and fail to differentiate terminally [2], giving rise to four subtypes named embryonal, alveolar, pleo- morphic, and spindle cell/sclerosing, each identified by distinctive ge- netic, histological and clinical features [3]. The main embryonal and alveolar forms are diagnosed in children under the age of 10 years and in adolescents or young adults, respectively. Embryonal tumors are often characterized by the loss of heterozygosity at chromosome 11p15.5 [4] and activation of the receptor tyrosine kinase/RAS/ERK axis [5], which plays a key role in the tumor growth [6–9], radioresistance [10–12] and metastasis [13]. Alveolar tumors are in-stead dominated by the t(2;13)(q35;q14) or t(1;13)(q36;q14) chromo- somal translocations, which are

responsible of the fusion of the paired box 3 and 7 (PAX3 and 7) genes and the 3′ end of the Forkhead box O1 (FOXO1) that generate the chimeric Pax3-FoxO1 or Pax7-FoxO1 on- coproteins, respectively [14]. Despite a multimodal therapy involving chemo- and radiotherapy and surgery can improve the prognosis in most cases, the occurrence of activating RAS mutations, the fusion- positive alveolar histology or the presence of metastases adversely in- fluence the survival rate of RMS patients [15,16]. We previously reported that Caveolin-1 (Cav-1), an ubiquitous protein belonging to a family of three highly conserved members (Cav-1, Cav-2 and Cav-3) [17], can promote tumor growth of embryonal RMS *in vitro* and *in vivo* [18–21]. Cav-1 is a scaffolding protein [22] with the ability to increase the biogenesis of caveolae, cholesterol-enriched microdomains of the plasma membrane involved in various cellular processes, such as me- chanical stress response [23], endocytosis [24], and signal transduction [25]. The role of Cav-1 in cancer appears to be complex, since its re- ported ability to modulate diverse cell signaling pathways [26] via the direct binding to a number of receptorial (G proteins, tyrosine-kinase receptors) and non-receptorial proteins (Src, H-Ras, endothelial NOS) mediated by a caveolin scaffolding domain [27]. Indeed, Cav-1 can either behave as a tumor suppressor or oncogene depending on many factors, including the tumor type and stage progression or the presence of post-translational modifications in its primary structure [28–30]. For example, loss of Cav-1 sensitizes to skin tumors in response to carci- nogen agents [31], whilst gain of Cav-1 expression is a poor predictor in prostate cancer [32]. Despite this, during advanced stages of cancer metastasis Cav-1 is reported to be often markedly expressed [33], as observed in gastric cancer [34] and melanoma cells [35], as well as to become phosphorylated by members of Src-kinase family [36] to activate pathways linked to cell survival [37]. For example, phosphorylated Cav-1 has been reported to influence focal adhesion dynamics through Src kinase and Rho GTPases, therefore enhancing cell polarization, directional migration and invasion in metastatic cancer cells [38–42]. As a result, the occurrence of phosphorylated Cav-1 is thought to predict unfavorable outcome by correlating with anchorage-independent cell growth, migration, invasiveness and multidrug resistance. In this work, by using a gain of function approach we demonstrated through an ex- perimental *in vivo* metastasis assay that Cav-1 facilitates the dissemination of the embryonal RD tumor cells through cooperation with Erk signaling.

2. Materials and methods

Reagents and antibodies were respectively from Sigma-Aldrich (Milan, Italy) and Santa Cruz Biotechnology (Dallas, TX, USA), unless otherwise stated.

2.1. *Antibodies*

The primary antibodies were rabbit polyclonal anti-Cav-1 (code sc- 894), mouse monoclonal anti-phosphorylated Cav-1 (Tyr14) (code 611338, BD Biosciences, Buccinasco, Italy), goat polyclonal anti-CD31 (sc-1506), mouse monoclonal anti-total Erk1/2 (code sc-135900), mouse monoclonal anti-phosphorylated Erk1/2 (Tyr204) (code sc- 7383), mouse monoclonal anti-MyoD (code sc-377460), rabbit poly- clonal anti-Caspase-3 (code NB100-56113, Novus Biological Europe, Abingdon, UK), mouse monoclonal anti-Myogenin (code sc-12732), mouse monoclonal anti-MHC (code sc-32732), mouse monoclonal anti- beta-Tubulin (code MA5-16308, Thermo Scientific, Rockford, USA). The secondary antibodies were anti-mouse (code sc-516102) and anti- rabbit (code sc-2357) IgG-HRP.

2.2. *Cell culture*

Human embryonal RD cells were purchased from the European Collection of Cell Cultures (ECACC, Salisbury, UK) and cultured ac- cording to manufacturer instructions. RD cells engineered for Cav-1 overexpression (RD^{F0}) were established as described in Ref. [20]. Cells were routinely maintained at 37 °C,

5% CO_2 in high-glucose Dulbecco's modified eagle's medium (DMEM) supplemented with 10% fetal bovine serum (FBS) (Life Technologies, Monza, Italy) and 100 mg/ml peni- cillin/streptomycin antibiotics. To induce myogenic differentiation, 80% confluent cells were switched to a medium composed by DMEM supplemented with 2% horse serum (HS) (Life Technologies, Monza, Italy).

2.3. *In vivo studies*

Animal experimental protocols were approved by the University of Brescia animal care committee (OPBA, Organismo Preposto al Benessere degli Animali) and were in accordance with national guide- lines and regulations. Procedures involving animals and their care were conformed with institutional guidelines that comply with national and international laws and policies (EEC Council Directive 86/609, OJ L 358, 12 December 1987) and with "ARRIVE" guidelines (Animals in Research Reporting In Vivo Experiments). Subcutaneous tumors were established by performing flank injections with 3×10^6 human tumor cells (resuspended in 100 µl PBS) into randomly selected 7-week-old male NOD/SCID mice (Envigo, Huntingdon, UK). Tumor growth was measured twice a week using caliper and tumor volume (V) was cal- culated as follows: $V = (\text{length} \times \text{width}^2) \times 0.5$. At the endpoint mice were sacrificed and tumors were formalin-fixed and prepared for his- tology analysis. Experimental metastases were established by per- forming tail vein injection of 3×10^5 cells (resuspended in 100 µl PBS) into 7-week-old male NOD/SCID mice. At different time-points mice were sacrificed for counting the metastases under a dissecting micro- scope. Lungs were then formalin-fixed for histology analysis. The arisen metastases were isolated and cultured *in vitro* as cell lines by mechan- ical fragmentation and incubation in complete medium supplemented with 1 mg/ml collagenase I (3 h, 37 °C). Then, dissociated cells were plated in fresh complete medium in the presence of G418 antibiotic (0.5 mg/ml).

2.4. *Immunoblotting*

Cells were lysed in RIPA buffer, sonicated and centrifuged (10000×*g*, 10 min, 4 °C). Protein concentration was determined with the Bradford reagent and 30–50 µg of protein were separated by SDS-PAGE, transferred onto polyvinylidine (PVDF) membranes and blocked with tris buffered saline (TBS) with 1% Tween-20 (TBS-T) and 5% milk (15 min, RT) prior to incubation with primary antibody (overnight, 4 °C). After 1 h with HRP-conjugated secondary antibody, membranes were TBS-T washed and the resulting immunocomplexes were visua- lized using enhanced chemiluminescence reagent (GeneSpin, Milan, Italy). Immunoreactive bands were quantified using Gel Pro Analyzer 4 software (MediaCybernetics Inc, Rockville, MD, USA).

2.5. *Immunohistochemistry*

Formalin-fixed, paraffin-embedded tumor sections (2 µm) were de- paraffinized in xylene and rehydrated through a 100–95% ethanol gradient. Sections were stained with Hematoxylin and Eosin followed by a series of dehydration steps via ethanol washes, cleared with xylene and mounted using Safemount (Bio Optica, Milan, Italy). Heat induced epitope retrieval was done with EDTA buffer pH 8.0 (1 h, 98 °C) and 0.3% H_2O_2 was used to block endogenous peroxidases. Sections were then washed in TBS (pH 7.4) and incubated with the specific primary antibody diluted in TBS with 1% bovine serum albumin (BSA) (1 h, RT). Protein signal was revealed by ChemMATE EnVision HRP Labelled
Polymer system (DAKO, Glostrup, Denmark) followed by diamino- benzydine as chromogen and Hematoxylin as counterstain. After re- peating a series of dehydration steps via ethanol washes, sections were cleared with xylene and mounted using Safemount (Bio Optica, Milan, Italy). Images were acquired by an inverted light microscope (Olympus IX50; Olympus, Tokyo, Japan) using cellSens Software (Olympus, Tokyo, Japan).

2.6. *Crystal violet assay*

Cell proliferation and adhesion were quantified through measure- ment of crystal violet incorporation. Cells were seeded in 24-well plates (1.5×10^4) for the proliferation assay or in 6-well plates (1.2×10^5 cells) for the adhesion assay. At the indicated time-points cells were fixed with 3% paraformaldehyde (PFA)/PBS solution (20 min, 4 °C) and stained with crystal violet solution (0.2% crystal violet/20% methanol/PBS) (10 min, RT). Cells were washed and re- suspended in 1% sodium dodecyl sulfate (SDS)/phosphate buffered saline (PBS) solution. Plates were shaken until complete dissolution was achieved and then absorbance was measured by reading the plate at 595 nm emission wavelength.

2.7. *Neutral red assay*

Cell viability was quantified by measuring the incorporation of the neutral red dye. Cells were seeded in 96-well plates (1.5×10^3) and, at the indicated time-points, were incubated with neutral red solution (40 μg/ml) dissolved in DMEM with 5% FBS (2 h, 37 °C) before washing with neutral red destaining solution (50% ethanol/1% acetic glacial acid/49% deionized water). Absorbance was measured by reading the plate at 540 nm emission wavelengths.

2.8. *Giemsa staining*

Differentiated cells were fixed in methanol (2 h, 4 °C) and incubated with Giemsa reactive (4 h, RT). After PBS washes, images were acquired by an inverted light microscope (Olympus IX50; Olympus, Tokyo, Japan) using cellSens Software (Olympus, Tokyo, Japan).

2.9. *Immunofluorescence*

Cells were cultured onto 12 mm glass coverslips in 24-well plates (1.5×10^4) for the indicated time-points. Cells were fixed with 3% PFA/PBS (20 min, 4 °C), permeabilized with 0.1% Triton X-100/PBS (10 min, RT) and then blocked with 1% BSA/PBS with 0.1% sodium azide (30 min, RT). Cells were incubated with primary antibody (3 h, RT), washed and then incubated with secondary antibody (45 min, RT). Nuclei were counterstained with Hoechst dye (30 s, RT) and samples were mounted on slides using Mowiol mounting media. Images were acquired by a confocal microscope with photo-multiplier tube detectors (LSM 510 Meta; Carl Zeiss, Oberkochen, Germany) using the LSM510 Meta software (Carl Zeiss, Oberkochen, Germany). Alternatively, images were acquired by a fluorescence Axiovert microscope (Carl Zeiss, Oberkochen, Germany) using the ImagePro Plus software (Media Cybernetics, Inc. Rockville, MD, USA).

2.10. *Sprouting assay*

HUVEC cells were seeded in a 96-well round bottom plate (8×10^2) in M199 medium supplemented with 8% fetal calf serum (FCS) and 0.2% methylcellulose. After 24 h, formed spheroids were collected with a plastic Pasteur and allowed to settle by gravity in a falcon tube (about 30 spheroids for each experimental point were used). Medium was then removed, and spheroids were suspended in a fibrin gel (composed of fibrinogen dissolved in M199 medium without serum) supplemented with thrombin. After 1 min at RT, gel included spheroids were rapidly seeded in a 96-well plate before the gel was completely solid and si- multaneously their adhesion to the bottom of the plate was prevented. Sprouting was stimulated with 100 μl of pre-filtered (0.45 μm) condi- tioned medium collected from RD^{ctrl}, RD^{F0}, RD^{F1} and RD^{F2} cells that were previously seeded in 60 mm dishes (3×10^5) and incubated for 24 h in DMEM without FBS. Spheroids

were observed and all capillary- like sprouts originating from the core of an individual spheroid were counted.

2.11. *Wound healing assay*

Cells seeded in 6-well plates (2×10^5) formed confluent monolayers that were pre-treated for 2 h with 10 μM PD098059 or DMSO and then wounded by scraping the cells with a 200 μl-sterile micropipette tip. Images of wound healing were acquired at different time-points by an inverted light microscope (Olympus IX50; Olympus, Tokyo, Japan) using cellSens Software (Olympus, Tokyo, Japan). The extent of wound repair was quantified by measuring the healed area using ImageJ software. Results were presented as percentage of repaired area with respect to time 0 h.

2.12. *Boyden chamber assay*

Detached and suspended cells were pre-treated for 2 h with 10 μM PD098059 or DMSO and then seeded (8×10^5 cells/ml) in the upper portion of a boyden chamber separated from the lower compartment containing DMEM with 10% FBS added with 10 μM PD098059 or DMSO by a gelatin-coated PVP-free polycarbonate filter with 8 mm pore size (Costar, Cambridge, USA). After incubation at 37 °C for 2 h, migrated cells were stained with Diff-Quik (Dade-Behring, Milan, Italy). The number of migrated cells was quantified using ImageJ software.

2.13. *Spheroid assay*

Spheroid cell aggregates were prepared upon incubation in 20% methylcellulose medium for 24 h. Cell aggregates were then embedded into Cultrex® Reduced Growth Factor Basement Membrane Matrix and stimulated with 10% FCS in the presence of 10 μM PD098059 or DMSO. After 4 h, cell aggregates were photographed at 100× magnification using an Axiovert 200 M microscope and invasion was quantified by measuring the length and the area of cell sprouts invading the sur- rounding gel using ImageJ software.

2.14. *Statistical analysis*

The differences between the groups were analyzed by unpaired Student's *t* test and One-Way Anova test, using GraphPad Prism 5 software (GraphPad Software, San Diego, USA). Statements of sig- nificance were based on a *p-value* of less than 0.05.

3. Results

3.1. *Cav-1 overexpression enhances tumor growth and lung dissemination of embryonal RD cells*

To assess the role of Cav-1 in RMS metastasis we employed a cell model previously established in our laboratory, consisting of the human embryonal RD cells engineered for Cav-1 overexpression (hereafter referred to as RD^{F0}) [20,21]. As shown via immunoblotting, RD^{F0} cells showed an increase in the content of both total and Tyr^{14}-phosphory- lated Cav-1 (pCav-1) forms compared to control cells (RD^{ctrl}) trans- fected with an empty vector (Fig. 1A). RD^{F0} cells had a marked tu- morigenic potential as previously reported [20], since their subcutaneous injection in NOD/SCID mice gave rise to tumor masses that reached an average volume of $643.3 \pm 77.2\ mm^3$ in 21 days (Fig. 1B), while RD^{ctrl} cells formed a tumor with similar volume in 79 days (Fig. 1B). By performing an experimental *in vivo* metastasis assay through tail vein injection of a pre-determined number of cells (3×10^5), we observed that RD^{F0} cells promoted the formation of pulmonary metastases detectable after 9 weeks (Fig. 1C and D), which were characterized

by high Cav-1 staining (Fig. 1D). In contrast, no metastatic nodules were detected upon injection of RD^{ctrl} cells (Fig. 1C). The arisen metastases were isolated and cultured *in vitro* as cell lines before further injection, according to the experimental procedure illu- strated in Fig. 1E. By repeating this protocol twice, we derived the RD^{F1} and RD^{F2} cell lines (after 5 and 4 weeks, respectively), whose metastatic potential was compared to that of RD^{F0} and RD^{ctrl} cells by setting a new metastasis *in vivo* assay. After 5 weeks, we observed that RD^{F1} or RD^{F2} injection has led to a higher number of macrometastases compared to RD^{F0} and RD^{ctrl} (Fig. 1F), which promoted a significant increase in the lung weight (Fig. 1G). Furthermore, we detected an increasing CD31 expression in the nodules derived from RD^{F0}, RD^{F1} and RD^{F2} cells, suggesting that metastatic growth requires increased blood flow (Fig. 1H).

3.2. *Metastatic lines show a greater Erk-dependent cell proliferation, reduced survival in response to nutrient deprivation and impairment of myogenic differentiation*

Crystal violet assay performed over a time-course showed that all the metastatic lines proliferated very quickly *in vitro*, reaching a four- fold increased density after 96 h compared to RD^{ctrl} cells (Fig. 2A). In metastatic lines, the increase in both total and pCav-1 levels was cor- related to a marked increase in phosphorylated Erk1/2 (pErk1/2) levels as well as to a reduction in MyoD levels compared to RD^{ctrl} cells (Fig. 2B). We next evaluated the impact of Erk inhibition on cell pro- liferation. Following treatment with the synthetic PD098059 inhibitor, both the pERK1/2 levels (Fig. 2C) and cell proliferation (Fig. 2D) were significantly downregulated compared to untreated lines. Similar re- sults were observed in RD^{F1} cells (not shown). Since a sustained cell division requires high nutrient availability, we found that culturing the metastatic lines in a serum deprived medium for 48 h triggered a con- sistent cell detachment from the plate compared to RD^{ctrl} (Fig. 3A). In these conditions, the neutral red assay evidenced a clear decrease of cell viability in metastatic lines compared to RD^{ctrl} (Fig. 3B), which we correlated with an augmented cell apoptosis by immunoblotting de- tection of the increased cleaved caspase-3 form (Fig. 3C). We next evaluated the myogenic potential of the different lines. While after 4 days of differentiation RD^{ctrl} cells showed a partial cell elongation correlating with increased expression of myosin heavy chain (MHC), the metastatic lines were refractory to both changes in cell shape and expression of differentiation markers (Fig. 3D). Immunoblotting showed that the levels of Cav-1 and pErk1/2 maintained higher in metastatic lines even after 4 days of differentiation compared to RD^{ctrl}, correlating with a drastic reduction in MyoD, Myogenin and MHC ex- pression (Fig. 3E).

3.3. *Metastatic lines show altered cell shape and increased adhesion and angiogenic features*

Metastatic lines evidenced a clear increase in cell size characterized by a more elongated cell body compared to RD^{ctrl}, as detected by light microscopy (Fig. 4A). Immunofluorescence analysis showed that Cav-1 staining was incremented intracellularly in metastatic RD^{F0} and RD^{F2} lines compared to RD^{ctrl}, markedly localizing in the proximity of peri- nuclear regions (Fig. 4A and B). Furthermore, metastatic lines exhibited changes in cytoskeletal architecture, highlighted by staining the fila- mentous actin (F-actin) with a fluorescent phalloidin, which revealed a higher content of stress fibers compared to RD^{ctrl} cells (Fig. 4A). Similar results were observed in RD^{F1} cells (not shown). In RD^{F0} and RD^{F2} lines, the cell area was estimated to be 3 times larger than the control line, as calculated by quantification of phalloidin fluorescence (Fig. 4C). We then assessed whether these changes could affect cell adhesion, a fea- ture playing a key role during local invasion of circulating primary tumor cells, by performing a crystal violet assay over a time-course (30–180 min). After seeding the cells, we observed the adhesion capa- city of the metastatic RD^{F0}, RD^{F1} and RD^{F2} lines being two-times higher than the RD^{ctrl} cells already after 30 min (Fig. 4D). Given the robust capillary formation previously observed in metastases *in vivo* (Fig. 1H), we tested the angiogenic potential of metastatic lines by a three-di- mensional sprouting assay on human endothelial cells (HUVEC) spheroids. Results showed HUVEC cells treated with the conditioned medium derived from RD^{F1} and RD^{F2}

cells formed a significantly in- creased number of angiogenic sprouts compared to RD^{F0} and RD^{ctrl} lines (Fig. 4E).

3.4. *Metastatic lines show enhanced Erk-dependent migration and invasiveness*

Wound healing and Boyden chamber assays were used to evaluate cell motility. In the first assay, we scratched a cell monolayer with a tip and captured light microscopy images. While after 8 h RD^{ctrl} cells repaired about 26% of the lesioned area, the metastatic lines repaired a double area (52,3% for RD^{F0}, 51,9% for RD^{F1} and 49,3% for RD^{F2}) (Fig. 5A and B). The repair capacity in both metastatic and control lines was overcome of about 20% in the presence of PD098059 inhibitor, suggesting that Erk pathway influenced cell migration (Fig. 5A and B). By means of a chemotaxis Boyden chamber assay we next confirmed these data, as the number of cells migrated through the membrane was significantly higher in metastatic lines than control cells already after 2 h, reaching a 2.3-fold increase for RD^{F0}, RD^{F1} and 1.7-fold increase for RD^{F2} (Fig. 5C). As already observed, the PD098059 treatment led to a 40% reduction in the migratory ability of the different lines (Fig. 5C). We then tried to detect if there were differences in the invasion capacity of the different metastatic lines, as observed *in vivo*. Since this requires an augmented ability to invade surrounding tissues by degradation of extracellular matrix, we performed a tumor spheroid invasion assay that provides the advantage for tumor cells to grow into a three-di- mensional structure (fibrin gel matrix) mimicking a tumor micro-region or a micro-metastasis [43]. As shown in Fig. 5D, all metastatic spher- oids, mainly those derived from the RD^{F2} line, showed a marked sprouting capacity following treatment with 10% fetal calf serum (FCS) compared to control spheroids. Based on these preliminary results, we monitored the magnitude of tumor invasion after 4 h by measuring both the spheroid area (blue line) and the sprout length (red line) to calcu- late the invasion area in the presence or absence of PD098059 (Fig. 5E). We found that the invasion area in all metastatic spheroids, identified as the area enclosed between the red and blue lines (Fig. 5E), was in- creased of about 10-fold compared to RD^{ctrl} (Fig. 5F). In addition, we observed a significant 30% reduction of the invasion area in RD^{F2} line treated with PD098059 (Fig. 5F). As shown in Fig. 5E, the sprout length of all metastatic lines was higher than RD^{ctrl} line and was reduced by treatment with PD098059. By performing the sprout length quantification, we confirmed that RD^{F0} and RD^{F1} or RD^{F2} spheroids formed sprouts that were increased of about 10-fold and 15-fold in comparison to RDctrl spheroids, respectively (Fig. 5G). Furthermore, the sprouting capacity of RD^{F1} or RD^{F2} spheroids was significantly 30% higher than RDF0 spheroids (Fig. 5G), accounting for the different observed ability to disseminate in vivo, and PD098059 treatment reduced the sprout length in RD^{F1} and RD^{F2} spheroids of about 30% compared to untreated spheroids (Fig. 5G).

4. Discussion

Metastatic dissemination is the leading cause of death in cancer patients. For RMS patients long-term survival for metastatic tumors remains low, being $<$ 20% for alveolar and 60% for embryonal sub- types [44]. The identification of molecular targets eliciting metastasis dissemination is therefore a challenge to improve current RMS ther- apeutic regimens. Over the past years we have demonstrated that Cav-1 is preferentially expressed in embryonal RMS tumors featured by a poor degree of myogenic differentiation [18]. In addition, we found that its increased or decreased expression in human engineered embryonal RD cells facilitates or dampens tumor growth *in vitro* and *in vivo*, respectively [20,21]. Here, by means of an experimental metastasis assay, we found that the increased Cav-1 levels can also facilitate the metastatic dissemination of embryonal RMS. Metastasis process in- volves four major steps: detachment of cancer cells from their primary loci, their entry into circulation (intravasation), their exit from circu- lation (extravasation), and survival and growth in a distant organ site [45]. In this regard, it is important to underline that our experimental model based on the intravenous injection of cancer cells provides a means to

evaluate organ colonization by cancer cells rather than the overall metastatic process [46]. However, the aggressive metastatic lines we generated are useful tools for identifying genes or molecular pathways related to metastatic progression of embryonal RMS.

The mechanisms by which Cav-1 enhances embryonal tumor pro- gression are currently unknown. Given the documented ability of Cav-1 to drive increased biogenesis of caveolae and accelerate the flow of nutrients (mostly glucose and fatty acids) across the membrane, as observed in particular in adipocytes [47,48], we cannot rule out that a similar mechanism may favor the rapid expansion of metastatic RMS lines. According to this, after nutrient deprivation the metastatic lines were characterized by a marked cell death compared to parental cells, a hallmark commonly detected in cells featured by high metabolic de- mands, such as tumor cells indeed [49]. Our data convincingly suggest a critical role for Cav-1 in facilitating the Erk signaling, even if the precise mechanisms through which this occurs remain to be addressed. Indeed, although Cav-1 has first been described in epithelial CHO cells to act as a negative regulator of Erk pathway by direct binding to Erk1/ 2 proteins [50], in other cell models it was reported to act as a positive regulator, as observed in colon cancer cells [51] or in metastatic Ewing sarcoma lines [52]. Elevated Erk signaling is a master driver of em- bryonal [7] and pleomorphic RMS [53] formation. Among the multi- tude of functions, the Erk pathway also plays a prominent role in overwhelming the differentiation capacity of RMS cells through me- chanisms that mediate MyoD inactivation [54,55] and repression of Myogenin expression [56]. Consistent with this, the established meta- static RD^{F0}, RD^{F1} and RD^{F2} lines were characterized by low expression of MyoD (already during cell proliferation) and Myogenin, and loss of differentiation capacity. These data therefore suggest that the co- operation between Cav-1 and the Erk signaling may support increased tumorigenic properties through the maintenance of a dedifferentiated state. Interestingly, CAV-1 was indicated as one of the five genes (BMP4, MYF5, DLK1, PAX7, CAV-1) that predict the occurrence of undifferentiated pleomorphic sarcoma (UPS) [57], which are more aggressive variants than embryonal RMS, lacking consistent histolo- gical, immunohistochemical, ultrastructural, or molecular markers [57]. Dedifferentiation is a hallmark found in metastases that are commonly enriched in cancer stem cells (CSCs), the cell subpopulation having the intrinsic ability to self-renew and propagate the entire in- tratumor heterogeneity [58]. Commonly, as long as tumor progresses, differentiation markers are lost and stem/progenitor markers become predominantly expressed due to cell enrichment in CSCs. To establish whether Cav-1 expression through Erk cooperation could dictate a dedifferentiation program in embryonal RMS, it will be important to characterize whether the enrichment in stem/progenitor markers could occur in three-dimensional RD^{F1} and RD^{F2} rhabdospheroids. Our data also indicate that Cav-1 through Erk signaling positively influences migration and invasiveness of metastatic RD lines. However, it is im- portant to underline that the different metastatic lines, though ex- hibiting increasing metastatic properties (RD^{F2} and RD^{F1} lines were more invasive than RD^{F0} as determined *in vivo* and by tumor spheroid assay), showed similar levels in the Erk pathway activation, indicating that additional pathways contribute to enhanced metastatic potential. Consistent with this, the synthetic Erk inhibition in the metastatic lines was not sufficient to fully abrogate the migratory and invasive prop- erties. In this regard, we found Cav-1 to be tyrosine-phosphorylated, and this mechanism known to be dependent on Src-kinase family members [20] has been recently proposed to redistribute the protein in the cytosolic compartments in order to facilitate the interaction with intracellular partners [59]. Since we actually found Cav-1 mainly lo- calizing in intracellular compartments of RD cells away from the plasma membrane, it is reasonable to think that the intracellular accumulation of pCav-1 might be responsible for the modulation of pro-migratory and pro-invasive pathways. In this context, pCav-1 has been documented to enhance migration and invasion in metastatic cancer cells by influen- cing focal adhesions [38–42]. These large, dynamic protein complexes
are made up by several proteins, including integrins, vinculin, talin, α- actinin, and focal adhesion kinase (FAK), through which intracellular actin bundles of a cell connects to the extracellular matrix during cell adhesion, morphogenesis and mechanotransduction processes [60]. In view of the changes in cell size and shape observed in RMS metastatic lines, we cannot rule out the possibility that pCav-1 may influence the

stress fibers dynamics to increase the migratory and invasive properties. To date, FAK inhibition was reported to decrease tumorigenic proper- ties in different embryonal and alveolar RMS cell lines [61]. Hence, the availability of highly metastatic RMS lines provides a unique tool to validate the potential relationship between pCav-1 and focal adhesions over the dissemination process.

In conclusion, our data suggest that an increase in Cav-1 expression levels can shape the tumor cell phenotype in embryonal RMS through persistent cell proliferation and loss of differentiation together with cytoskeletal reorganization underlying increased cell motility. Further investigation is required to identify the additional Cav-1 downstream pathways contributing to metastasis dissemination.

Conflicts of interest

We have no conflict of interest to declare.

Author contributions

SC, FF, and AF planned experiments.
SC, FF, RR, PC, EG, MG performed experiments. SC, FF, RR, FMe, FMa, and AF analyzed data. AF wrote the paper.

Acknowledgements

This work was supported by the University of Brescia (ex 60%) and Siderurgica Leonessa research funds to AF. RR was supported by Associazione Italiana per la Ricerca sul Cancro - AIRC (MFAG 18459 grant). We are grateful to Umberto Veronesi Foundation for granting FMa with Post-doctoral Fellowship year-2018 Award. We acknowledge Luigi Poliani and Manuela Cominelli for assistance in tumor samples inclusion.

References

[1] D.M. Parham, F.G. Barr, Classification of rhabdomyosarcoma and its molecular basis, Adv. Anat. Pathol. 20 (2013) 387–397.
[2] C. Keller, D.C. Guttridge, Mechanisms of impaired differentiation in rhabdomyo- sarcoma, FEBS J 280 (2013) 4323–4334.
[3] C.D.M. Fletcher, J.A. Bridge, P.C.W. Hogendoorn, F. Mertens, WHO Classification of Tumours of Soft Tissue and Bone, IARC, Lyon, 2013.
[4] J. Anderson, A. Gordon, A. McManus, J. Shipley, K. Pritchard-Jones, Disruption of imprinted genes at chromosome region 11p15.5 in paediatric rhabdomyosarcoma, Neoplasia 1 (1999) 340–348.
[5] J.F. Shern, L. Chen, J. Chmielecki, J.S. Wei, R. Patidar, M. Rosenberg, L. Ambrogio, D. Auclair, J. Wang, Y.K. Song, C. Tolman, L. Hurd, H. Liao, S. Zhang, D. Bogen, A.S. Brohl, S. Sindiri, D. Catchpoole, T. Badgett, G. Getz, J. Mora, J.R. Anderson, S.X. Skapek, F.G. Barr, M. Meyerson, D.S. Hawkins, J. Khan, Comprehensive genomic analysis of rhabdomyosarcoma reveals a landscape of alterations affecting a common genetic axis in fusion-positive and fusion-negative tumors, Cancer Discov. 4 (2014) 216–231.
[6] C.M. Linardic, D.L. Downie, S. Qualman, R.C. Bentley, C.M. Counter, Genetic modeling of human rhabdomyosarcoma, Cancer Res. 65 (2005) 4490–4495.
[7] D.M. Langenau, M.D. Keefe, N.Y. Storer, J.R. Guyon, J.L. Kutok, X. Le, W. Goessling, D.S. Neuberg, L.M. Kunkel, L.I.C.P. Zon, Effects of RAS on the genesis of embryonal rhabdomyosarcoma, Genes Dev. 21 (2007) 1382–1395.
[8] F. Marampon, C. Ciccarelli, B.M. Zani, Down-regulation of c-Myc following MEK/ ERK inhibition halts the expression of malignant phenotype in rhabdomyosarcoma and in non muscle-derived human tumors, Mol. Canc. 5 (2006) 31.
[9] F. Marampon, G. Bossi, C. Ciccarelli, A. Di Rocco, A. Sacchi, R.G. Pestell, B.M. Zani, MEK/ERK

inhibitor U0126 affects in vitro and in vivo growth of embryonal rhab- domyosarcoma, Mol. Canc. Therapeut. 8 (2009) 543–551.
[10] F. Marampon, G.L. Gravina, A. Di Rocco, P. Bonfili, M. Di Staso, C. Fardella, L. Polidoro, C. Ciccarelli, C. Festuccia, V.M. Popov, R.G. Pestell, V. Tombolini, B.M. Zani, MEK/ERK inhibitor U0126 increases the radiosensitivity of rhabdo- myosarcoma cells in vitro and in vivo by downregulating growth and DNA repair signals, Mol. Canc. Therapeut. 10 (2011) 159–168.
[11] G.L. Gravina, C. Festuccia, V.M. Popov, A. Di Rocco, A. Colapietro, P. Sanità, S.D. Monache, D. Musio, F. De Felice, E. Di Cesare, V. Tombolini, F. Marampon, c- Myc sustains transformed phenotype and promotes radioresistance of embryonal rhabdomyosarcoma cell lines, Radiat. Res. 185 (2016) 411–422.
[12] C. Ciccarelli, F. Vulcano, L. Milazzo, G.L. Gravina, F. Marampon, G. Macioce, A. Giampaolo, V. Tombolini, V. Di Paolo, H.J. Hassan, B.M. Zani, Key role of MEK/ ERK pathway in sustaining tumorigenicity and in vitro radioresistance of embryonal rhabdomyosarcoma stem-like cell population, Mol. Canc. 15 (2016) 16.
[13] M. Saini, A. Verma, S.J. Mathew, SPRY2 is a novel MET interactor that regulates metastatic potential and differentiation in rhabdomyosarcoma, Cell Death Dis. 9 (2018) 237.
[14] F.G. Barr, N. Galili, J. Holick, J.A. Biegel, G. Rovera, B.S. Emanuel, Rearrangement of the PAX3 paired box gene in the paediatric solid tumour alveolar rhabdomyo- sarcoma, Nat. Genet. 3 (1993) 113–117.
[15] X. Chen, E. Stewart, A.A. Shelat, C. Qu, A. Bahrami, M. Hatley, G. Wu, C. Bradley, J. McEvoy, A. Pappo, S. Spunt, M.B. Valentine, V. Valentine, F. Krafcik, W.H. Lang, M. Wierdl, L. Tsurkan, V. Tolleman, S.M. Federico, C. Morton, C. Lu, L. Ding, J. Easton, M. Rusch, P. Nagahawatte, J. Wang, M. Parker, L. Wei, E. Hedlund, D. Finkelstein, M. Edmonson, S. Shurtleff, K. Boggs, H. Mulder, D. Yergeau, S. Skapek, D.S. Hawkins, N. Ramirez, P.M. Potter, J.A. Sandoval, A.M. Davidoff, E.R. Mardis, R.K. Wilson, J. Zhang, J.R. Downing, M.A. DyerS.J.C.s.R.H.W.U.P.C.G. Project, Targeting oxidative stress in embryonal rhabdomyosarcoma, Cancer Cell 24 (2013) 710–724.
[16] S.X. Skapek, J. Anderson, F.G. Barr, J.A. Bridge, J.M. Gastier-Foster, D.M. Parham, E.R. Rudzinski, T. Triche, D.S. Hawkins, PAX-FOXO1 fusion status drives unfavor- able outcome for children with rhabdomyosarcoma: a children's oncology group report, Pediatr. Blood Canc. 60 (2013) 1411–1417.
[17] T.M. Williams, M.P. Lisanti, The caveolin proteins, Genome Biol. 5 (2004) 214.
[18] S. Rossi, P.L. Poliani, M. Cominelli, A. Bozzato, R. Vescovi, E. Monti, A. Fanzani, Caveolin 1 is a marker of poor differentiation in Rhabdomyosarcoma, Eur. J. Cancer 47 (2011) 761–772.
[19] S. Rossi, P.L. Poliani, C. Missale, E. Monti, A. Fanzani, Caveolins in rhabdomyo- sarcoma, J. Cell Mol. Med. 15 (2011) 2553–2568.
[20] F. Faggi, S. Mitola, G. Sorci, F. Riuzzi, R. Donato, S. Codenotti, P.L. Poliani, M. Cominelli, R. Vescovi, S. Rossi, S. Calza, M. Colombi, F. Penna, P. Costelli, I. Perini, M. Sampaolesi, E. Monti, A. Fanzani, Phosphocaveolin-1 enforces tumor growth and chemoresistance in rhabdomyosarcoma, PLoS One 9 (2014) e84618.
[21] F. Faggi, N. Chiarelli, M. Colombi, S. Mitola, R. Ronca, L. Madaro, M. Bouche, P.L. Poliani, M. Vezzoli, F. Longhena, E. Monti, B. Salani, D. Maggi, C. Keller, A. Fanzani, Cavin-1 and Caveolin-1 are both required to support cell proliferation, migration and anchorage-independent cell growth in rhabdomyosarcoma, Lab Invest 95 (2015) 585–602.
[22] M. Sargiacomo, P.E. Scherer, Z. Tang, E. Kübler, K.S. Song, M.C. Sanders, M.P. Lisanti, Oligomeric structure of caveolin: implications for caveolae membrane organization, Proc. Natl. Acad. Sci. U. S. A. 92 (1995) 9407–9411.
[23] B. Sinha, D. Köster, R. Ruez, P. Gonnord, M. Bastiani, D. Abankwa, R.V. Stan, G. Butler-Browne, B. Vedie, L. Johannes, N. Morone, R.G. Parton, G. Raposo, P. Sens, C. Lamaze, P. Nassoy, Cells respond to mechanical stress by rapid dis- assembly of caveolae, Cell 144 (2011) 402–413.
[24] J.P. Cheng, B.J. Nichols, Caveolae: one function or many? Trends Cell Biol. 26 (2016) 177–189.
[25] R.G. Parton, M.A. del Pozo, Caveolae as plasma membrane sensors, protectors and organizers, Nat. Rev. Mol. Cell Biol. 14 (2013) 98–112.

[26] C. Boscher, I.R. Nabi, Caveolin-1: role in cell signaling, Adv. Exp. Med. Biol. 729 (2012) 29–50.
[27] J. Couet, S. Li, T. Okamoto, T. Ikezu, M.P. Lisanti, Identification of peptide and protein ligands for the caveolin-scaffolding domain. Implications for the interaction of caveolin with caveolae-associated proteins, J. Biol. Chem. 272 (1997) 6525–6533.
[28] E. Burgermeister, M. Liscovitch, C. Röcken, R.M. Schmid, M.P. Ebert, Caveats of caveolin-1 in cancer progression, Cancer Lett. 268 (2008) 187–201.
[29] J.G. Goetz, P. Lajoie, S.M. Wiseman, I.R. Nabi, Caveolin-1 in tumor progression: the good, the bad and the ugly, Cancer Metastasis Rev. 27 (2008) 715–735.
[30] M. Sáinz-Jaspeado, J. Martin-Liberal, L. Lagares-Tena, S. Mateo-Lozano, X. Garcia del Muro, O.M. Tirado, Caveolin-1 in sarcomas: friend or foe? Oncotarget 2 (2011) 305–312.
[31] F. Capozza, T.M. Williams, W. Schubert, S. McClain, B. Bouzahzah, F. Sotgia, M.P. Lisanti, Absence of caveolin-1 sensitizes mouse skin to carcinogen-induced epidermal hyperplasia and tumor formation, Am. J. Pathol. 162 (2003) 2029–2039.
[32] T.M. Williams, G.S. Hassan, J. Li, A.W. Cohen, F. Medina, P.G. Frank, R.G. Pestell, D. Di Vizio, M. Loda, M.P. Lisanti, Caveolin-1 promotes tumor progression in an autochthonous mouse model of prostate cancer: genetic ablation of Cav-1 delays advanced prostate tumor development in tramp mice, J. Biol. Chem. 280 (2005) 25134–25145.
[33] J. Ketteler, D. Klein, Caveolin-1, cancer and therapy resistance, Int. J. Cancer 143 (2018) 2092–2104.
[34] E. Burgermeister, X. Xing, C. Röcken, M. Juhasz, J. Chen, M. Hiber, K. Mair, M. Shatz, M. Liscovitch, R.M. Schmid, M.P. Ebert, Differential expression and function of caveolin-1 in human gastric cancer progression, Cancer Res. 67 (2007) 8519–8526.
[35] S. Guerrero, V.M. Díaz-García, P. Contreras-Orellana, P. Lara, S. Palma, F. Guzman, L. Lobos-Gonzalez, A. Cárdenas, X. Rojas-Silva, L. Muñoz, L. Leyton, M.J. Kogan, A.F. Quest, Gold nanoparticles as tracking devices to shed light on the role of ca- veolin-1 in early stages of melanoma metastasis, Nanomedicine 13 (2018) 1447–1462.
[36] S. Li, R. Seitz, M.P. Lisanti, Phosphorylation of caveolin by src tyrosine kinases. The alpha-isoform of caveolin is selectively phosphorylated by v-Src in vivo, J. Biol. Chem. 271 (1996) 3863–3868.
[37] A.F. Quest, L. Lobos-González, S. Nuñez, C. Sanhueza, J.G. Fernández, A. Aguirre, D. Rodríguez, L. Leyton, V. Torres, The caveolin-1 connection to cell death and survival, Curr. Mol. Med. 13 (2013) 266–281.
[38] A. Grande-García, A. Echarri, J. de Rooij, N.B. Alderson, C.M. Waterman-Storer, J.M. Valdivielso, M.A. del Pozo, Caveolin-1 regulates cell polarization and direc- tional migration through Src kinase and Rho GTPases, J. Cell Biol. 177 (2007) 683–694.
[39] B. Joshi, S.S. Strugnell, J.G. Goetz, L.D. Kojic, M.E. Cox, O.L. Griffith, S.K. Chan, S.J. Jones, S.P. Leung, H. Masoudi, S. Leung, S.M. Wiseman, I.R. Nabi, Phosphorylated caveolin-1 regulates Rho/ROCK-dependent focal adhesion dy- namics and tumor cell migration and invasion, Cancer Res. 68 (2008) 8210–8220.
[40] F. Meng, S. Saxena, Y. Liu, B. Joshi, T.H. Wong, J. Shankar, L.J. Foster, P. Bernatchez, I.R. Nabi, The phospho-caveolin-1 scaffolding domain dampens force fluctuations in focal adhesions and promotes cancer cell migration, Mol. Biol. Cell 28 (2017) 2190–2201.
[41] M. Nethe, P.L. Hordijk, A model for phospho-caveolin-1-driven turnover of focal adhesions, Cell Adhes. Migrat. 5 (2011) 59–64.
[42] J.G. Goetz, B. Joshi, P. Lajoie, S.S. Strugnell, T. Scudamore, L.D. Kojic, I.R. Nabi, Concerted regulation of focal adhesion dynamics by galectin-3 and tyrosine-phos- phorylated caveolin-1, J. Cell Biol. 180 (2008) 1261–1275.
[43] M. Vinci, C. Box, S.A. Eccles, Three-dimensional (3D) tumor spheroid invasion assay, JoVE (2015) e52686.
[44] S. Hettmer, Z. Li, A.N. Billin, F.G. Barr, D.D. Cornelison, A.R. Ehrlich, D.C. Guttridge, A. Hayes-Jordan, L.J. Helman, P.J. Houghton, J. Khan, D.M. Langenau, C.M. Linardic, R. Pal, T.A. Partridge, G.K. Pavlath, R. Rota, B.W. Schäfer, J. Shipley, B. Stillman, L.H. Wexler, A.J. Wagers, C. Keller, Rhabdomyosarcoma: current challenges and their implications for developing therapies, Cold Spring Harb

Perspect Med 4 (2014) a025650.
[45] M. Saxena, G. Christofori, Rebuilding cancer metastasis in the mouse, Mol Oncol 7 (2013) 283–296.
[46] S. Mohanty, L. Xu, Experimental metastasis assay, JoVE 24 (2010) pii: 1942.
[47] M. Yamamoto, Y. Toya, C. Schwencke, M.P. Lisanti, M.G. Myers, Y. Ishikawa, Caveolin is an activator of insulin receptor signaling, J. Biol. Chem. 273 (1998) 26962–26968.
[48] B.L. Trigatti, R.G. Anderson, G.E. Gerber, Identification of caveolin-1 as a fatty acid binding protein, Biochem. Biophys. Res. Commun. 255 (1999) 34–39.
[49] E. Monti, A. Fanzani, Uncovering metabolism in rhabdomyosarcoma, Cell Cycle 15 (2016) 184–195.
[50] J.A. Engelman, C. Chu, A. Lin, H. Jo, T. Ikezu, T. Okamoto, D.S. Kohtz, M.P. Lisanti, Caveolin-mediated regulation of signaling along the p42/44 MAP kinase cascade in vivo. A role for the caveolin-scaffolding domain, FEBS Lett. 428 (1998) 205–211.
[51] U.K. Basu Roy, R.S. Henkhaus, F. Loupakis, C. Cremolini, E.W. Gerner,
N.A. Ignatenko, Caveolin-1 is a novel regulator of K-RAS-dependent migration in colon carcinogenesis, Int. J. Cancer 133 (2013) 43–57.
[52] L. Lagares-Tena, S. García-Monclús, R. López-Alemany, O. Almacellas-Rabaiget,
J. Huertas-Martínez, M. Sáinz-Jaspeado, S. Mateo-Lozano, C. Rodríguez-Galindo,
S. Rello-Varona, D. Herrero-Martín, O.M. Tirado, Caveolin-1 promotes Ewing sar- coma metastasis regulating MMP-9 expression through MAPK/ERK pathway, Oncotarget 7 (2016) 56889–56903.
[53] H. Tsumura, T. Yoshida, H. Saito, K. Imanaka-Yoshida, N. Suzuki, Cooperation of oncogenic K-ras and p53 deficiency in pleomorphic rhabdomyosarcoma develop- ment in adult mice, Oncogene 25 (2006) 7673–7679.
[54] S.J. Tapscott, M.J. Thayer, H. Weintraub, Deficiency in rhabdomyosarcomas of a factor required for MyoD activity and myogenesis, Science 259 (1993) 1450–1453.
[55] Z. Yang, K.L. MacQuarrie, E. Analau, A.E. Tyler, F.J. Dilworth, Y. Cao, S.J. Diede, S.J. Tapscott, MyoD and E-protein heterodimers switch rhabdomyosarcoma cells from an arrested myoblast phase to a differentiated state, Genes Dev. 23 (2009) 694–707.
[56] M.E. Yohe, B.E. Gryder, J.F. Shern, Y.K. Song, H.C. Chou, S. Sindiri, A. Mendoza, R. Patidar, X. Zhang, R. Guha, D. Butcher, K.A. Isanogle, C.M. Robinson, X. Luo, J.Q. Chen, A. Walton, P. Awasthi, E.F. Edmondson, S. Difilippantonio, J.S. Wei, K. Zhao, M. Ferrer, C.J. Thomas, J. Khan, MEK inhibition induces MYOG and re- models super-enhancers in RAS-driven rhabdomyosarcoma, Sci. Transl. Med. 10 (2018).
[57] B.P. Rubin, K. Nishijo, H.I. Chen, X. Yi, D.P. Schuetze, R. Pal, S.I. Prajapati, J. Abraham, B.R. Arenkiel, Q.R. Chen, S. Davis, A.T. McCleish, M.R. Capecchi, J.E. Michalek, L.A. Zarzabal, J. Khan, Z. Yu, D.M. Parham, F.G. Barr, P.S. Meltzer, Y. Chen, C. Keller, Evidence for an unanticipated relationship between un- differentiated pleomorphic sarcoma and embryonal rhabdomyosarcoma, Cancer Cell 19 (2011) 177–191.
[58] J.E. Visvader, G.J. Lindeman, Cancer stem cells: current status and evolving com- plexities, Cell Stem Cell 10 (2012) 717–728. [59] A.M. Zimnicka, Y.S. Husain, A.N. Shajahan, M. Sverdlov, O. Chaga, Z. Chen, P.T. Toth, J. Klomp, A.V. Karginov, C. Tiruppathi, A.B. Malik, R.D. Minshall, Src- dependent phosphorylation of caveolin-1 Tyr-14 promotes swelling and release of caveolae, Mol. Biol. Cell 27 (2016) 2090–2106.
[60] S. Tojkander, G. Gateva, P. Lappalainen, Actin stress fibers–assembly, dynamics and biological roles, J. Cell Sci. 125 (2012) 1855–1864.
[61] A.M. Waters, L.L. Stafman, E.F. Garner, S. Mruthyunjayappa, J.E. Stewart, E. Mroczek-Musulman, E.A. Beierle, Targeting focal adhesion kinase suppresses the malignant phenotype in rhabdomyosarcoma cells, Transl Oncol 9 (2016) 263–273.

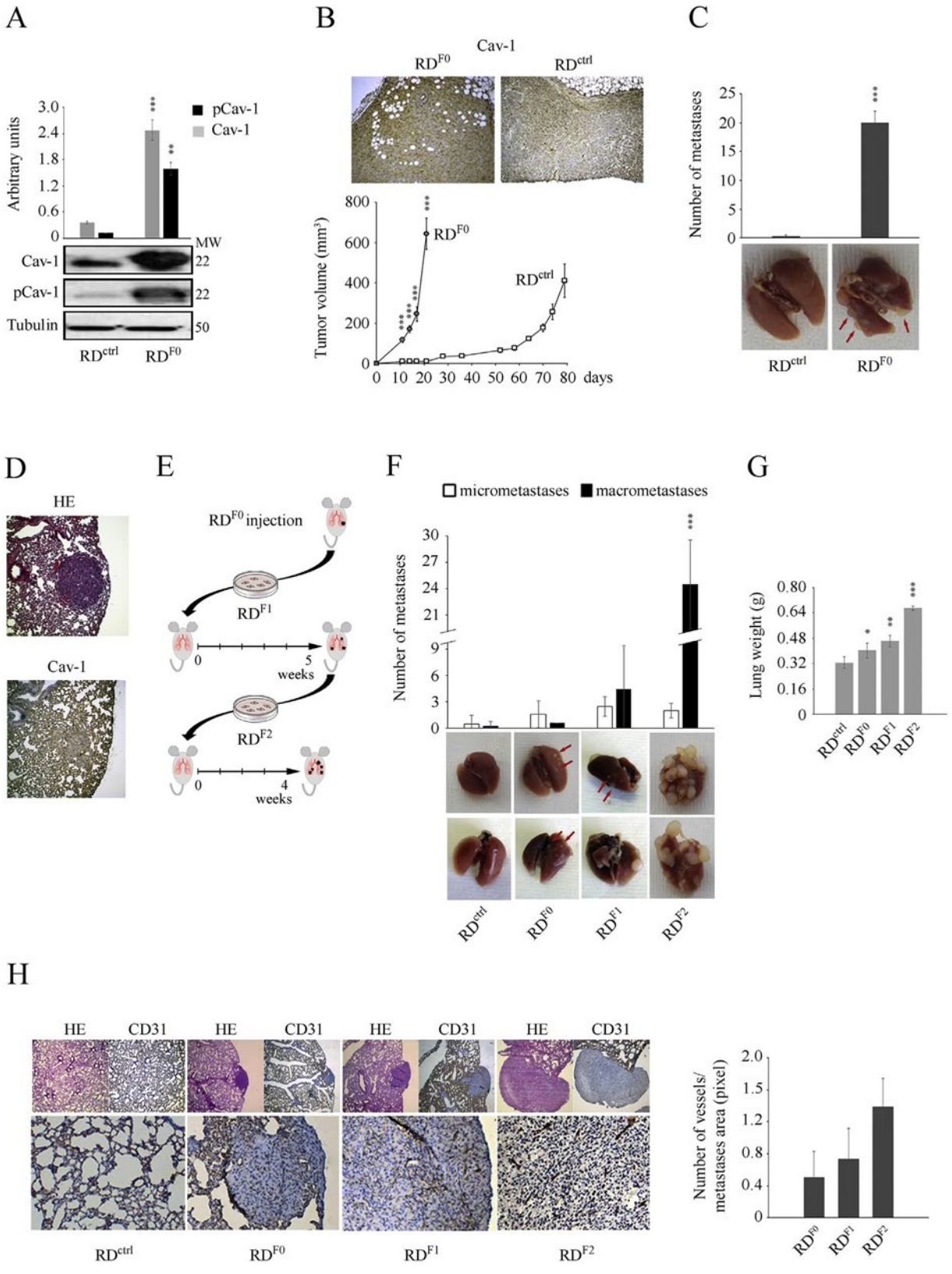

Fig. 1. Cav-1 overexpression enhances lung dissemination of embryonal RD cells. A) Immunoblotting was performed on total protein homogenates derived from human RDctrl and RDF0 cells collected after 24 h of cell proliferation. Protein bands quantification was obtained using tubulin as a loading control (n = 4). Data are Mean ± SEM, ** p-value < 0.001; *** p-value <

0.0001; unpaired Student's t-test. B) Volumetric measurement of xenografted tumors by caliper (n = 8). Cav-1 staining was revealed in tumor xenografts by immunohistochemistry (top images, 10×). Data are Mean ± SEM, *** p-value < 0.0001; unpaired Student's t-test. C) Metastatic nodules on the lungs, indicated by red arrows, were quantified after intravenous cell injection of RDctrl and RDF0 lines (n = 6). Data are Mean ± SEM, *** p-value < 0.0001; unpaired Student's t-test. D) Images (10×) show the lung metastases processed by Hematoxylin and Eosin (HE) staining or by immunohistochemistry for Cav-1 staining. It should be noted that the Cav-1 staining in metastases is masked by equally high expression in the surrounding lung fibroblasts. E) As depicted schematically, the metastases arisen in the lungs of injected mice were cultured in vitro to derive the RDF1 and RDF2 lines. F) Images show the micrometastases (arrows) and macrometastases detectable in the lungs of mice injected with RDctrl, RDF0, RDF1, and RDF2 cells after 5 weeks. The number of lung nodules was quantified (n = 16). Data are Mean ± SEM, *** p-value < 0.0001; One-Way Anova test. G) The lungs of the mice injected with the different lines were weighed (n = 16). Data are Mean ± SEM, * p-value < 0.05; ** p-value < 0.001; *** p-value < 0.0001; One-Way Anova test. H) Images (4× and 20×) show lung metastases processed by Hematoxylin and Eosin (HE) staining or by immunohistochemistry for CD31 staining. Lung tissue from RDctrl-injected mice was used as control. The number of vessels was quantified with respect to the metastases area (n = 3). (For interpretation of the references to colour in this figure legend, the reader is referred to the Web version of this article.)

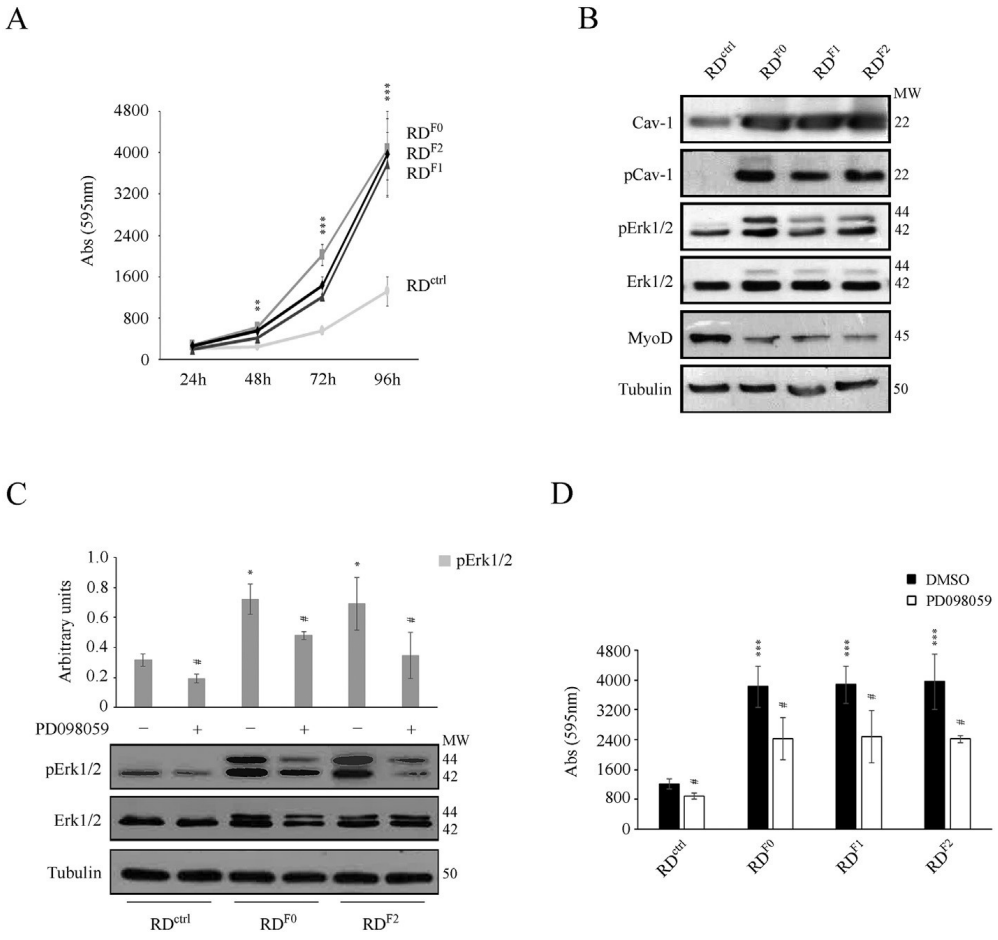

Fig. 2. Metastatic lines show Erk-dependent increase in cell proliferation. A) Crystal violet assay was performed to evaluate cell proliferation over a time- course (n = 4). Data are Mean ± SEM, ** *p-value* < 0.001; *** *p-value* < 0.0001; One-Way Anova test. B) Immunoblotting was performed on total protein homogenates collected after 48 h of cell proliferation (n = 4). C) Immunoblotting was per- formed on total protein homogenates collected after 72 h of cell proliferation in the presence of 10 μM PD098059 or DMSO. Protein bands quantification was obtained using tubulin as a loading control. The ratio of pErk1/2 was quantified to total protein (n = 4). Data are Mean ± SEM, * *p-value* < 0.05 *vs* RD^{ctrl} cells; One-Way Anova test. # *p-value* < 0.05 *vs* DMSO-treated cells; unpaired Student's t-test. D) In the conditions seen above, crystal violet assay was performed (n = 4). Data are Mean ± SEM, *** *p- value* < 0.0001 *vs* RD^{ctrl} cells; One-Way Anova test. # *p-value* < 0.05 *vs* DMSO-treated cells; unpaired Student's t-test.

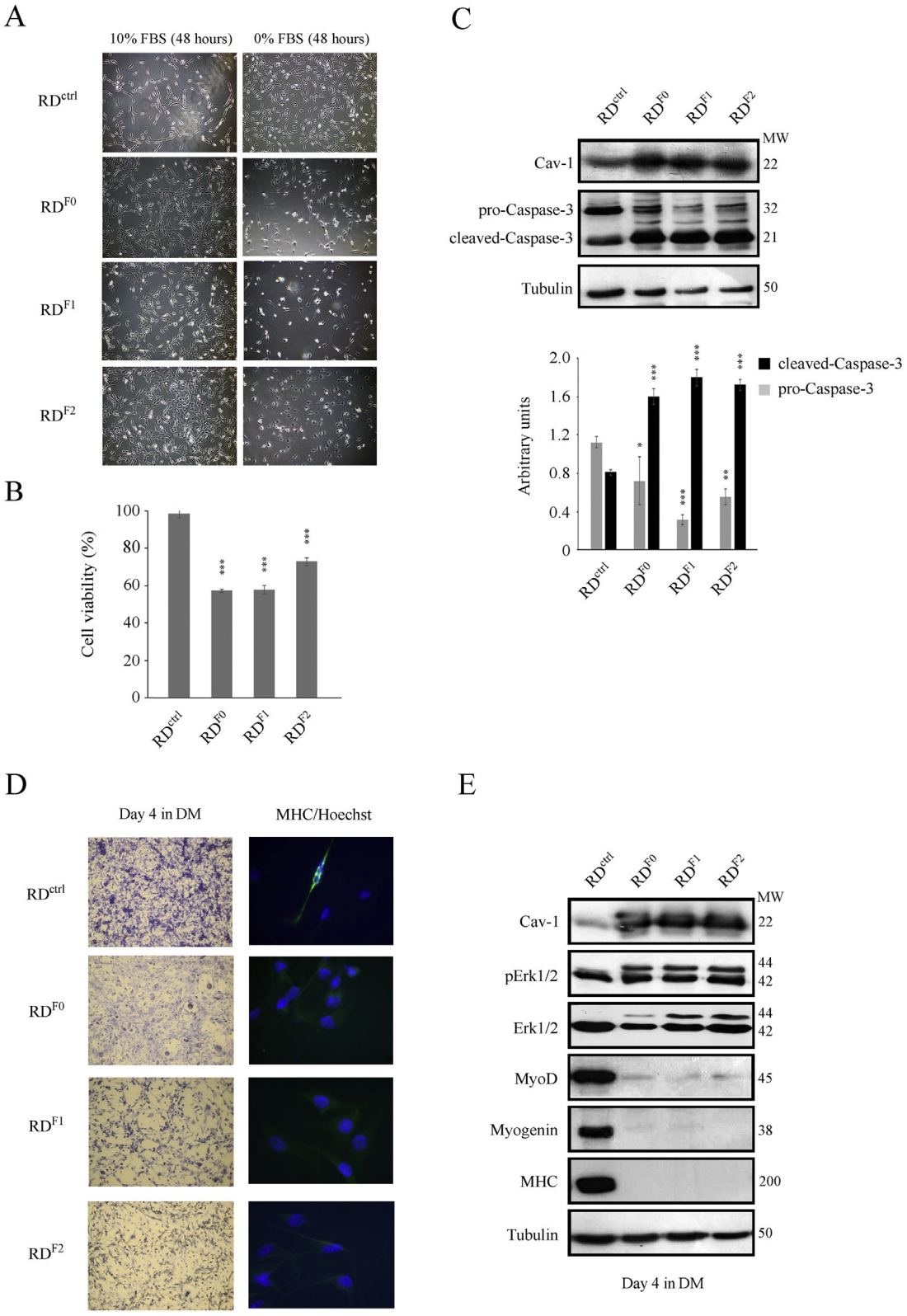

Fig. 3. Metastatic lines are characterized by a marked cell apoptosis in response to nutrient deprivation and a drastic impairment of the myogenic potential. A) The different cell lines were seeded and maintained in complete medium (10% FBS) for 24 h. Then, cells were either maintained in 10% FBS or in a serum free medium (0% FBS) for additional 48 h (n = 3). Images (10×) highlight the robust cell detachment of the metastatic lines in the absence of serum compared to RD^{ctrl} line. B) In the conditions

seen above, neutral red assay was performed (n = 3). Data are Mean ± SEM, *** *p-value* < 0.0001; One-Way Anova test. C) Immunoblotting was performed on total cell homogenates collected after 48 h of serum deprivation. Protein bands quantification was obtained using tubulin as a loading control (n = 3). Data are Mean ± SEM, * *p-value* < 0.05; ** *p-value* < 0.001; *** *p-value* < 0.0001; One-Way Anova test. D) The cell lines were maintained in differentiation medium (DM) for 4 days. Images show the cells processed by Giemsa staining (4×) or immunofluorescence for MHC staining (63×) (n = 3). E) In the same conditions seen above, immunoblotting was performed on total cell homogenates. Tubulin was used as a loading control (n = 3). (For interpretation of the references to colour in this figure legend, the reader is referred to the Web version of this article.)

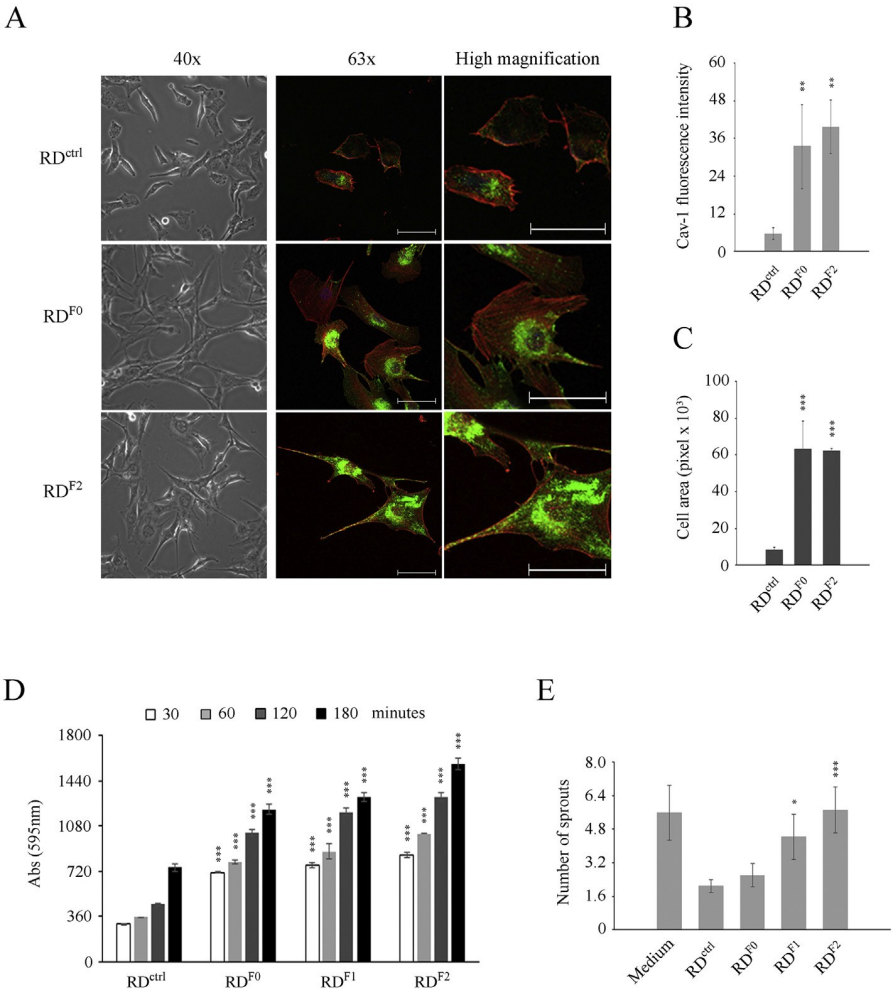

Fig. 4. Metastatic lines show altered cytoskeleton architecture and enhanced adhesion and angiogenic potential. A) Light microscopy images (40×) high- light the different morphology of metastatic RD^{F0} and RD^{F2} lines compared to RD^{ctrl}, as detected after 48 h of cell proliferation (n = 3). Confocal micro- scopy images (63×) show the different lines pro- cessed by immunofluorescence for Cav-1 (green) and phalloidin (red) staining (n = 3). The scale bar corresponds to 50 μm. B) The intensity of Cav-1 fluorescence was quantified using the ImagePro Plus software (n = 3). Data are Mean ± SEM, ** *p-value* < 0.001; One-Way Anova test. C) The cell area was calculated according to the phalloidin fluores- cence using the ImagePro Plus software (n = 3). Data are Mean ± SEM, *** *p-*

value < 0.0001; One- Way Anova test. D) Crystal violet assay was per- formed to evaluate the adhesion capacity at the in- dicated time-points (n = 3). Data are Mean ± SEM,
*** *p-value* < 0.0001; One-Way Anova test. E) HUVEC sprouting assay was performed to assess the angiogenic potential. The number of sprouts was quantified for each cell line. Complete medium was used as positive control (n = 2). Data are Mean ± SEM, * *p-value* < 0.05; *** *p-value* < 0.0001; One-Way Anova test. (For interpretation of the references to colour in this figure legend, the reader is referred to the Web version of this article.)

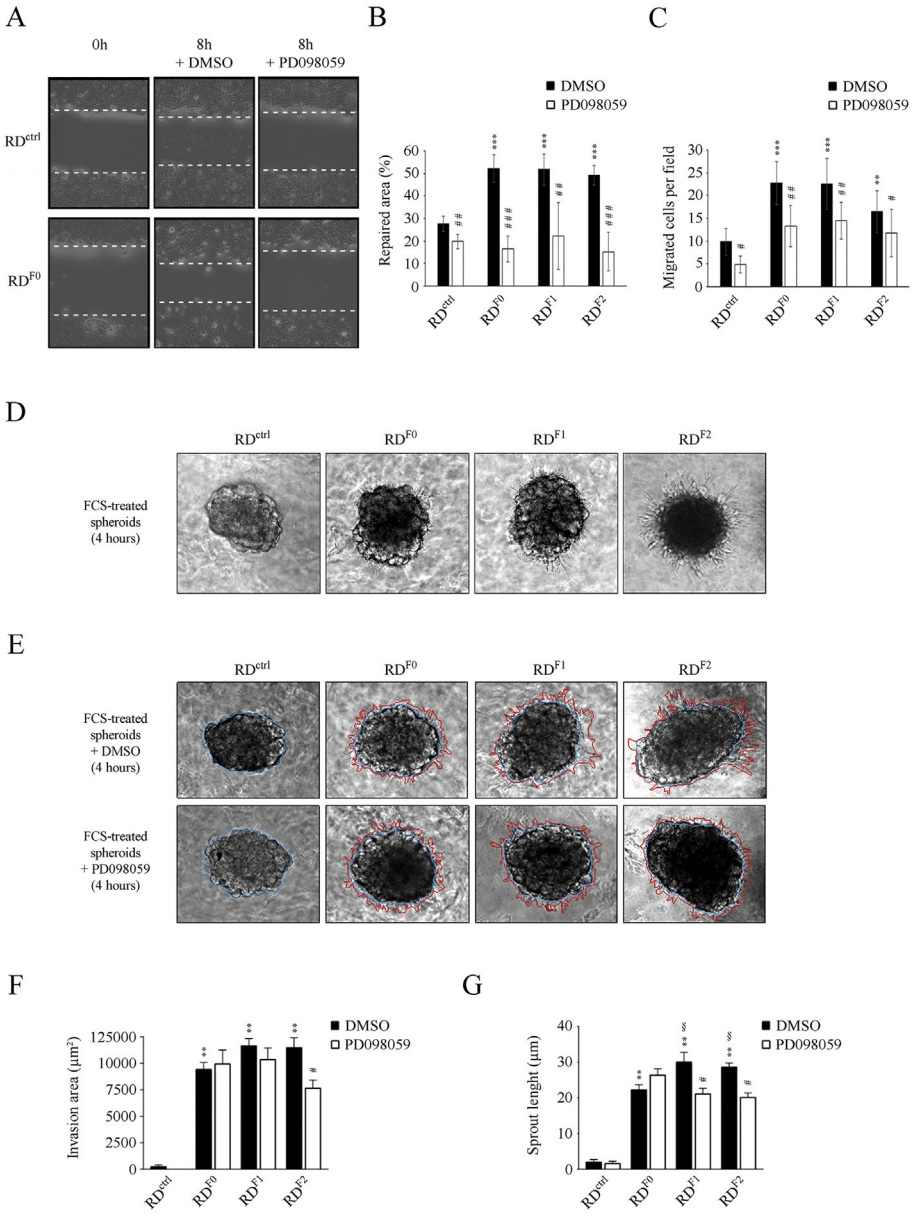

Fig. 5. Metastatic lines show enhanced Erk-depen- dent migration and invasion. A) Wound healing assay was performed to test the ability of the dif- ferent lines to repair the injured area in the presence of 10 μM PD098059 or DMSO. The dotted white line identifies the migration front. Images (10×) were taken after 8 h. B) The repaired area was quantified using ImageJ software (n = 4). Data are Mean ± SEM, *** *p-value* < 0.0001 *vs* RD^{ctrl} cells; One-Way Anova test. # # *p-value* < 0.001; # # # *p- value* < 0.0001 *vs* DMSO-treated cells; unpaired Student's t-test. C) Boyden chamber assay was per-
formed to evaluate the migratory ability of the var- ious lines after 2 h of incubation with 10 μM PD098059 or DMSO. The number of migrated cells was quantified using ImageJ software (n = 3). Data are Mean ± SEM, ** *p-value* < 0.001; *** *p- value* < 0.0001 *vs* RD^{ctrl} cells; One-Way Anova test. # *p-value* < 0.05; # # *p-value* < 0.001 *vs* DMSO- treated cells; unpaired Student's t-test. D) Images (100×) representative of the various tumor spher- oids embedded into a fibrin gel matrix and stimulated for 4 h with FCS to evaluate the sprouting capacity. E) In the conditions seen above, the invasion and sprouting capacity of the various spheroids was evaluated in the presence of 10 μM PD098059 or DMSO. Images (100×) show the spheroid area and the sprout length respectively highlighted by the blue and the red lines (n = 3). F-G) Quantification of the invasion area (evaluated as the area enclosed between the two lines) (F) and of the sprout length (G) using ImageJ software. Data are Mean ± SEM, ** *p-value* < 0.001 *vs* RD^{ctrl} cells; One-Way Anova test. # *p-value* < 0.05; *vs* DMSO-treated cells; unpaired Student's t-test. § *p-value* < 0.05 *vs* RD^{F0}; One- Way Anova test. (For interpretation of the references to colour in this figure legend, the reader is referred to the Web version of this article.)